Computational Modeling of Electrohydrodynamically-Influenced Mercury Adsorption within ESPs

Herek L. Clack
Department of Civil and Environmental Engineering
University of Michigan
Ann Arbor, Michigan USA

hclack@umich.edu

ABSTRACT

Powdered activated carbon (PAC) injection into the flue gas at a location upstream of an electrostatic precipitator (ESP) has emerged as a leading technology capable of reaching the ~90% reduction in mercury emissions representing the performance target set by the U.S. EPA's new Mercury and Air Toxics Standard (MATS). The present study presents a newly developed 2-D numerical model of electrohydrodynamically-influenced trace gas adsorption within a simulated section of a wire-plate ESP. The results reveal fundamental details of the gas-particle dynamics and mass transfer enhancements that, along with powdered mercury sorbents and their chemical treatments, can enable efficient mercury adsorption within ESPs.

INTRODUCTION

The control of anthropogenic mercury emissions is a growing priority, with combustion – specifically coal-fired power plants (CFPPs) – as the largest remaining anthropogenic source. In 2012 the U.S. EPA issued the Mercury and Air Toxics Standard (MATS) [1] for electric utilities. Injection of powdered mercury sorbents, typically activated carbon, upstream of an existing particulate control device (PCD) has been among the most thoroughly tested of all mercury emissions control technologies. The widespread use of electrostatic precipitators (ESPs) in the U.S. (approximately 80% [2]) has meant that powdered activated carbon (PAC) injection upstream of an ESP has been a common configuration for reducing mercury emissions from CFPPs.

ESPs, somewhat understandably, have been only sparsely instrumented during full-scale PAC injection testing at electric utilities. Typically, such tests have reported a single measurement of mercury concentration each at the inlet and outlet of the ESP ($[Hg]_{in}$ and $[Hg]_{out}$, respectively), obtained over a period during which boiler load and PAC injection rate were held constant, although the mercury content of the coal can vary, resulting in varying $[Hg]_{in}$ (e.g., Figure 1). Only a few full-scale tests have acquired time-resolved $[Hg]_{out}$ measurements that could be used to characterize ESP-related phenomena. Several others have reported mercury concentrations in individual hoppers, each containing a mixture of fly ash and mercury sorbent collected in the associated ESP field above it. Such ash analyses can give a limited indication of gross mercury capture in the unit as a whole, by ESP field.

While progress has been made in recent years in fundamental modeling of particle collection within ESPs (e.g., [3]), similar modeling of adsorption of trace pollutants such as mercury within ESPs has until now, and with the exception of the work of the present investigator and co-workers [4-9], remained a mostly empirical engineering endeavor. A key distinction between particle collection simulations and trace pollutant adsorption simulations is evidence of at least two distinct

mass transfer mechanisms in the ESP that underlie the overall removal of mercury from the flue gas. The two mechanisms are Hg adsorption by suspended particles in the flue gas (in-flight) and by the collected particles comprising the dustcake on the collection electrodes (wall-bounded).

Figure 1 [10] shows evidence of the two mass transfer mechanisms through time-resolved $[Hg]_{in}$ and $[Hg]_{out}$ measurements at a utility ESP undergoing PAC injection testing. The bottom trace (red) is the PAC injection rate; the top trace (blue) is the ESP inlet mercury concentration, $[Hg]_{in}$, and the middle trace (pink) is the ESP outlet mercury concentration, $[Hg]_{out}$. Of particular interest is the nearly instantaneous drop in $[Hg]_{out}$ in response to PAC injection. This is in contrast to the gradual "recovery" of $[Hg]_{out}$ once PAC injection stops. Given that flue gas residence times within ESPs are on the order of seconds, the hours-long recovery evident at the end of PAC injection in Figure 1 leads to two conclusions: 1) the immediate drop in $[Hg]_{out}$ at the start of PAC injection is reflective of an in-flight mass transfer mechanism for mercury, and 2) the gradual recovery in $[Hg]_{out}$ once PAC injection stops represents a wall-bounded mass transfer mechanism in which mercury continues to be adsorbed by PAC retained on ESP surfaces (mixed with fly ash). The behaviors of $[Hg]_{in}$ and $[Hg]_{out}$ vary from site to site along with overall Hg removal.

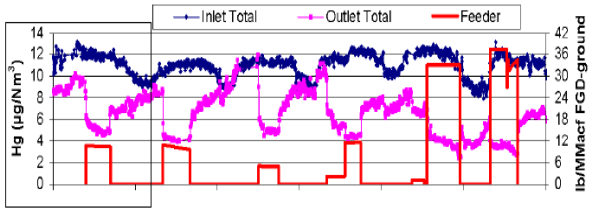

Figure 1. Measured total mercury concentrations and PAC injection rates during PAC injection testing at We Energies' Pleasant Prairie Power Plant (USA) [10]. Measured mercury concentrations at the ESP inlet (blue) and outlet (pink), with PAC injection rates in red.

However, better understanding of both is necessary if ESPs are to achieve the dual objectives of controlling emissions of both trace pollutants and particulate matter (PM). Despite more than a decade of U.S. experience, however, there is limited understanding of how mercury sorbents behave within ESPs, either in adsorbing mercury or their impacts on PM removal efficiency. The present study uses a multi-physics computational platform (COMSOL^{TM}) to compute 2-D electric fields, electrohydrodynamically-influenced fluid patterns and particle trajectories, and resulting PM and mercury removal efficiencies.

METHODOLOGY

The 2-D computational domain is a two-meter-long section of a wire-plate ESP. The section consists of three wire discharge electrodes (1 mm diameter, 0.5 m spacing) positioned along the centerline between two parallel planar collection electrodes (spacing 0.3 m). COMSOL^{TM} multi-physics software suite provides the computational platform. Separate modules solve for the electric field, electrohydrodynamically-influenced fluid flow field, charged particle motion, and mass transfer of trace concentrations of mercury from the gas phase to the adsorbing surfaces. In the section, subject to the voltage boundary conditions and an assumed space charge density distribution, the continuous phase flow field as governed by the Reynolds-averaged Navier-Stokes equations for air as the fluid:

$$\nabla \bullet \vec{u} = 0 \qquad (1)$$

$$\vec{u} \bullet \nabla \vec{u} = -\frac{1}{\rho}\nabla P + \nu \nabla^2 \vec{u} + q_i \nabla \Phi \qquad (2)$$

the momentum equation having been modified to include additional Coulombic body force terms in the x- and y-directions based on the computed local values of electric field and space charge density. In (1) and (2) above, $\bar{u}$ is the local gas velocity vector, P is pressure, ρ is the gas density, ν is the gas kinematic viscosity, q_i is the local space charge density, and Φ is the local electric potential (voltage). The electric field is computed directly by COMSOL^{TM},

however, the space charge density distribution in the section is determined through a separate manual iteration procedure conducted within the COMSOL™ environment in which an assumed spatial distribution of space charge density is applied, the electric field calculated, and charge conservation and current continuity:

$$\nabla^2 \Phi = -\frac{q_i}{\varepsilon} \tag{3}$$

$$\nabla \bullet \left(\left(b_i \nabla \Phi + \vec{u} \right) q_i + \alpha \nabla q_i \right) = 0 \tag{4}$$

are checked for consistency. Repeated iterations vary the function representing the space charge density distribution in the section until consistency is achieved; in cases where linear charge density of the discharge electrodes is known, such iterations also include comparisons of computed and specified linear charge density values. In (3) and (4) above, b_i is the ionic mobility in air, ε is the permittivity in air, and α is the diffusivity coefficient.

After solving for the electrohydrodynamically-influenced fluid flow field in the section, this solution is used as a solution initialization for a series of multi-phase mixture modules in which the transport of solid particles, including their loss to the collection electrodes and the mass transfer associated with adsorption of mercury to their collective surface, is calculated. The particles, representing injected powdered mercury sorbent, exist as a polydisperse suspension in the continuous phase. With the exception of bulk density, the electrical and physical properties of graphite were assigned to the particles, in the absence of detailed property data for such sorbents. The particles are present in the gas stream at the entrance to the section, having been injected into the gas stream at an upstream location and assumed to have been fully dispersed across the channel and uniformly distributed. Figure 2 shows the log-normal size distribution of the particles, having a mean particle diameter of 20 μm and a geometric standard deviation of 1.75. This continuous distribution was collected into 11 size bins (1.5, 2.5, 3.5, 7, 15, 25, 35, 45, 60, 85, 125 μm), each

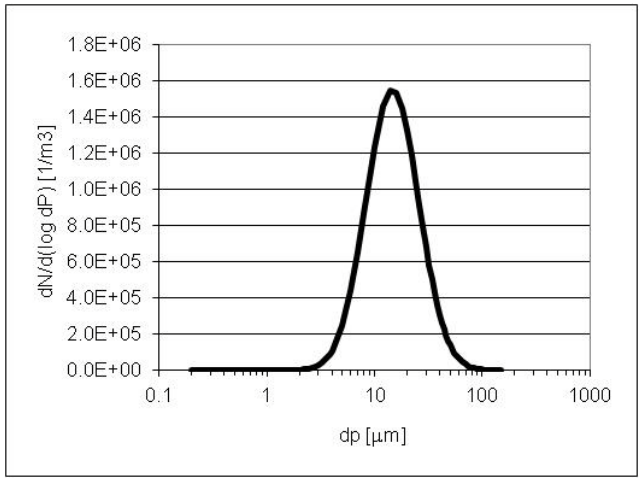

Figure 2. Assumed particle size distribution of powdered mercury sorbent. Mean diameter of 20 μm, geometric standard deviation of 1.75.

size bin treated in its own multi-phase mixture module computing particle slip velocity and convective mass transfer as a function of particle mass and acquired charge at saturation (particles are assumed to instantaneously achieve their saturated charge). The eleven multi-phase mixture modules then simultaneously solve for the collective mass transfer throughout the section over all particle sizes, accounting for particle removal to the collection electrodes and particle slip due to inertial, drag, and Coulombic forces. After the simultaneous solution of the multi-phase mixture modules, a module computing the transport and reaction of dilute chemical species then calculates the change in an initially uniform concentration (4e-7 mol/m^3) of mercury in response to the collective mass transfer thus computed.

For wall-bounded mercury adsorption, the multi-phase mixture modules are deactivated, replaced by a transport and reaction of dilute chemical species module in which the collection electrodes are defined as having zero mercury concentration at their surfaces and the mercury flux to these surfaces is then calculated by the module through convection and diffusion. This boundary condition is overly generous, however, with respect to actual conditions likely to exist during PAC injection because it treats the entire surface of the collection electrodes as

an adsorbing surface. In practice, the dustcake on the collection electrodes will contain only one or two percent of powdered mercury sorbent, the rest being (relatively) inert fly ash. Thus, the surface concentration boundary condition at the collection electrodes will be non-zero, decreasing the diffusive and convective mass transfer to those surfaces and the overall mercury removal efficiency. Despite this, the relative, rather than absolute, change in mercury concentration due to wall-bounded adsorption (i.e., calculated mercury removal efficiency, defined as $([Hg]_{in} - [Hg]_{out}) / [Hg]_{in}$) is illustrative in terms of revealing the effects of the EHD-influenced flow field.

RESULTS AND DISCUSSION

Two EHD conditions were considered for all results presented. A low-EHD condition was applied in which the fluid momentum was sufficiently high (or, equivalently, Coulombic forces were sufficiently low) as to minimize any large-scale "ionic wind" effects, and a high-EHD condition in which the effect of the ion transport was large enough to substantially alter the bulk fluid flow. For simplicity, the high- and low-EHD conditions differed in their inlet velocity boundary conditions (0.1 and 0.5 m/s, respectively) only, with all other conditions remaining constant. Figure 3 presents velocity fields in the section for both high- and low-EHD conditions. Velocity magnitude is indicated by the color mapping, overlain by streamlines. For the low-EHD condition, intermittent regions of substantially higher (up to 0.75 m/s) and lower (as low as 0.1 m/s) velocities are apparent in the flow field that, in the absence of an electric field, would be expected to show continuous development of low velocity boundary layers along the collection electrodes and accelerating fluid velocities nearer the centerline as the flow becomes fully developed. By contrast, the high-EHD condition shows much more pronounced flow disruption with repeated recirculation patterns throughout the flow, also characterized by regions having velocities substantially higher and lower than the inlet value.

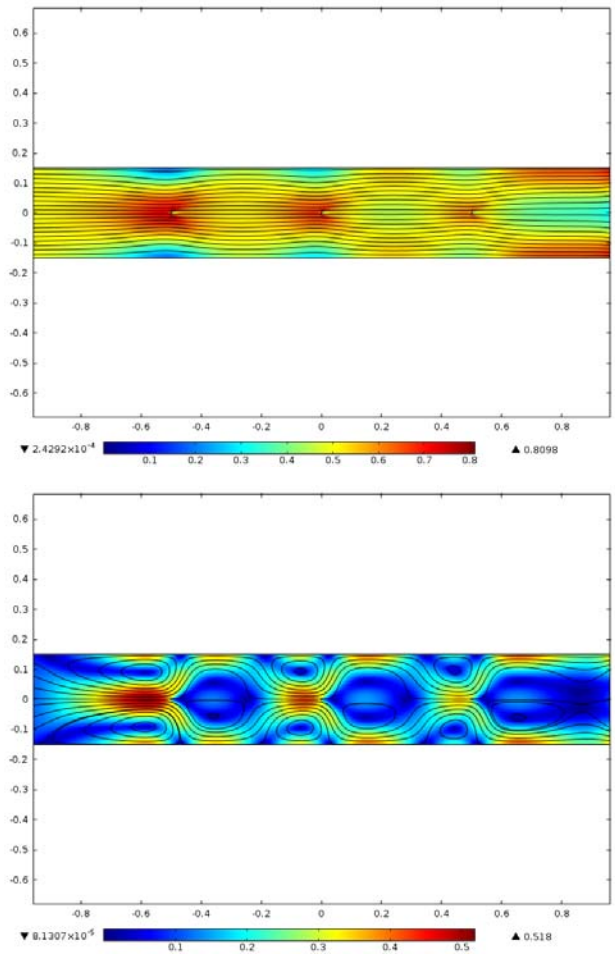

Figure 3. Computed fluid streamlines and velocities for electro-hydrodynamically induced air flow (left to right) within a simulated 2-D ESP channel containing three wire discharge electrodes energized to 70 kV, T = 180 ^{o}C. Upper: U_0 = 0.5 m/s. Lower: U_0 = 0.1 m/s.

With these fluid flow fields as a context, Figure 4 presents the wall-bounded mercury adsorption modeling results. For the low-EHD condition (Figure 4, upper), species transport occurs through the velocity and concentration boundary layers developing over the collection electrodes that exhibit only minor influences of the electric field; perturbations of the mercury concentration boundary layer correlate with the localized

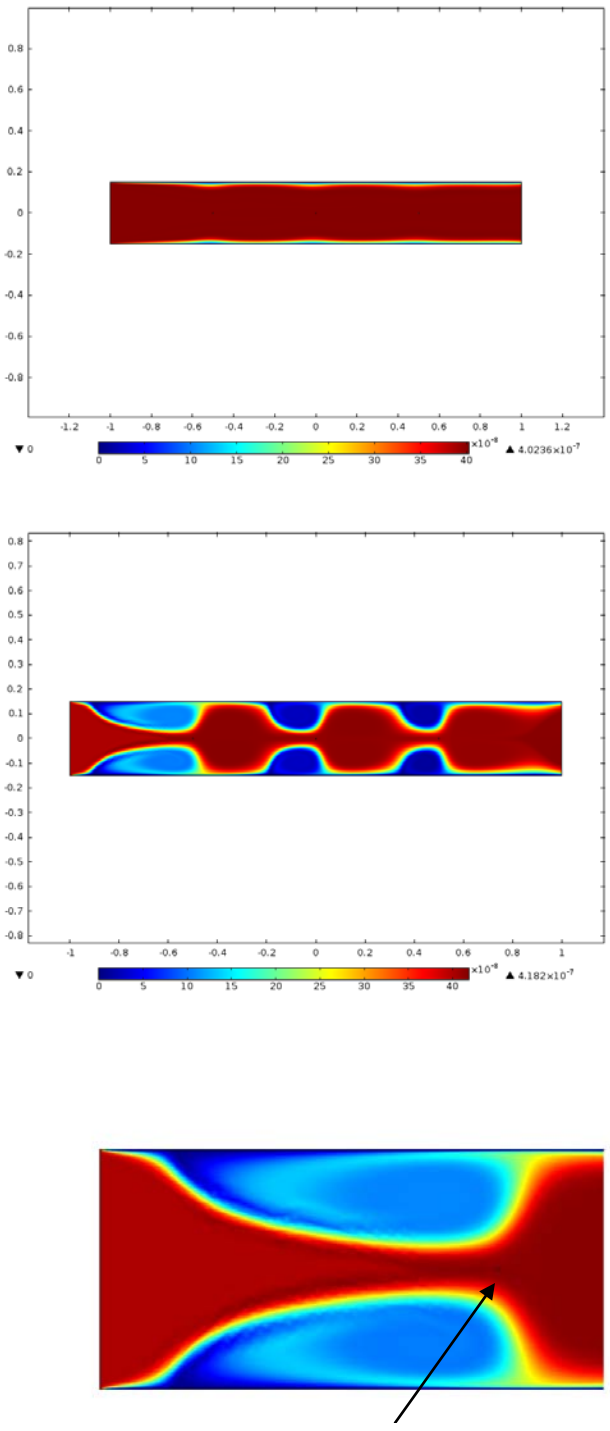

Figure 4. Computed distributions of mercury concentration for wall-bounded adsorption only. V_0 = 70 kV, T = 180 ^oC. Upper: Low-EHD condition, U_0 = 0.5 m/s. Center: High-EHD condition, U_0 = 0.1 m/s; Lower: Detail of inlet at high-EHD condition. Air flows from left to right.

expansion of the velocity boundary layers evident in the low-EHD flow field plot. Integrating the mercury fluxes at the inlet and outlet of the section under high- and low-EHD conditions, the mercury removal efficiency under low-EHD conditions is 8.3% as compared to 32.2% for the high-EHD condition. As noted earlier, the homogeneous wall boundary condition ($[Hg]_{wall}$ = 0) for the wall-bounded solutions overpredicts the mass transfer and resulting mercury removal efficiency; however, the relative difference between low- and high-EHD conditions is remarkable, indicating a nearly four-fold increase in mass transfer as a result of the high-gradient regions produced by the recirculation zones.

Figures 5 and 6 present the results from the multi-phase mixture modeling of the polydisperse mercury sorbent particles suspended in the gas. Figure 5 shows the distribution of particle number density in the section for the largest (125 μm) and smallest (1.5 μm) particles considered in the size distribution. Because the adsorption of mercury by the suspended particles occurs currently with the removal of the particles from the gas stream, the selected particle number density distributions shown in Figure 5 give insight into the regions of high particle number density, regions that would correspond to high rates of mercury adsorption and lead to lower downstream mercury concentrations in the section.

Figure 6 shows the distribution of mercury concentration within the ESP section under high- and low-EHD conditions. The greatest rate of mercury removal is at the section inlet where all particle number densities are highest, then generally decreasing with downstream distance as particles are removed from the gas flow. The spatial variation in mercury concentration is less pronounced under the low-EHD condition (Figure 6, upper), absent the large-scale recirculation zones present in the high-EHD condition. For the low-EHD condition, integration of mercury flux at the section inlet and outlet indicates a mercury

removal efficiency of approximately 1.55% for this 2 m-long section. Aside from the incorporation of detailed adsorption kinetics, these results likely underpredict full-scale results because of the assumption that all particles enter the section bearing their saturation charge; allowing a charge accumulation period for the particles will result in lower particle removal rates near the section inlet, providing all particles with longer in-flight times during which mercury adsorption can occur. Considering the variation of mercury concentration under low-EHD conditions (Figure 6, upper), there appears to exist a central region of relatively higher mercury concentrations that persists throughout the section. This is likely the result of 1) the flow acceleration that is evident along the section centerline (see Figure 3, upper), and 2) the early depletion of sorbent particles along the streamline, a region that receives no particles drifting toward the collection electrodes. It is interesting to note that the regions of low mercury concentration along the collection electrodes are not the result of mercury adsorption by the collected material comprising the dustcake, as these results (Figure 6) consider only mercury adsorption by suspended particles. Thus, the regions of low mercury concentration along the section walls likely reflect the negligible values of the y-components of both the particle drift velocity (due to the electric field near the wall) and bulk gas velocity (due to mass continuity constraints at the wall). This region of lower mercury concentration persists throughout the section due to the continuous drift of fine particles into the near-wall region, and the absence of dispersive or diluting bulk fluid motion in this region.

In contrast, the high-EHD condition (Figure 6, lower) shows highly differentiated regions of mercury concentration, closely correlated with the large recirculation zones whose presence in the flow is evident in Figure 3 (lower). The recirculation zones generally represent regions of lower mercury concentration than are present

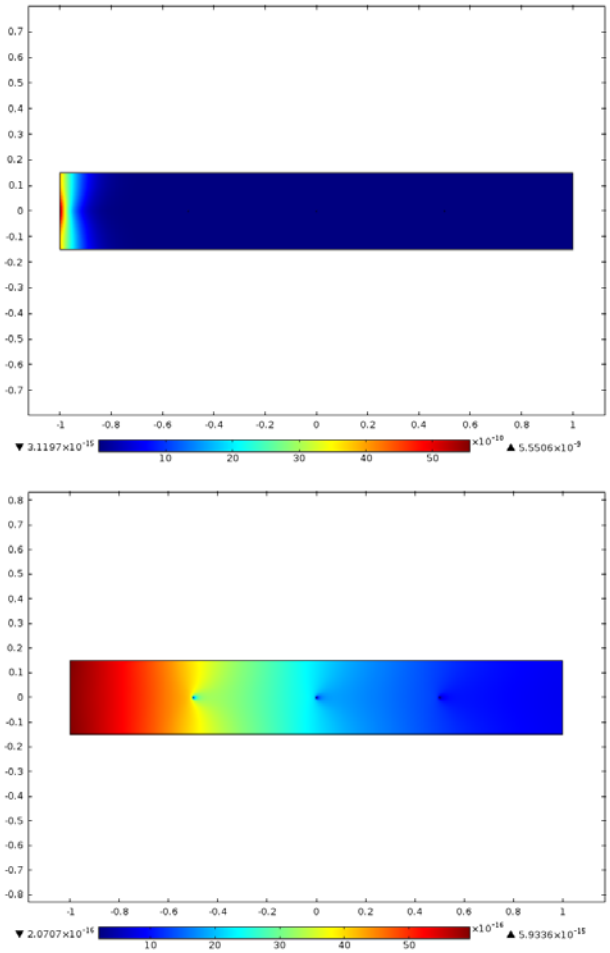

Figure 5. Selected particle number density distributions in ESP section under low-EHD conditions. Upper: 125 μm particle number density; particle removal efficiency of >99.99%. Lower: 1.5 μm particle number density; particle removal efficiency of 85.5%. Air flow is from left to right.

in the fluid "jet" that begins at the inlet along the section centerline and then diverges around the first discharge electrode towards each of the collection electrodes. Animations of computed particle paths (not shown) confirm the entrainment of suspended particles in the recirculation zones, where their in-flight residence times can be extended, allowing greater time for adsorption. However, the unabated process of particle removal from the gas stream as a whole diminishes this effect in downstream regions, with the second and third recirculation zone pairs (Figure 6, lower) showing increasing mercury concentrations,

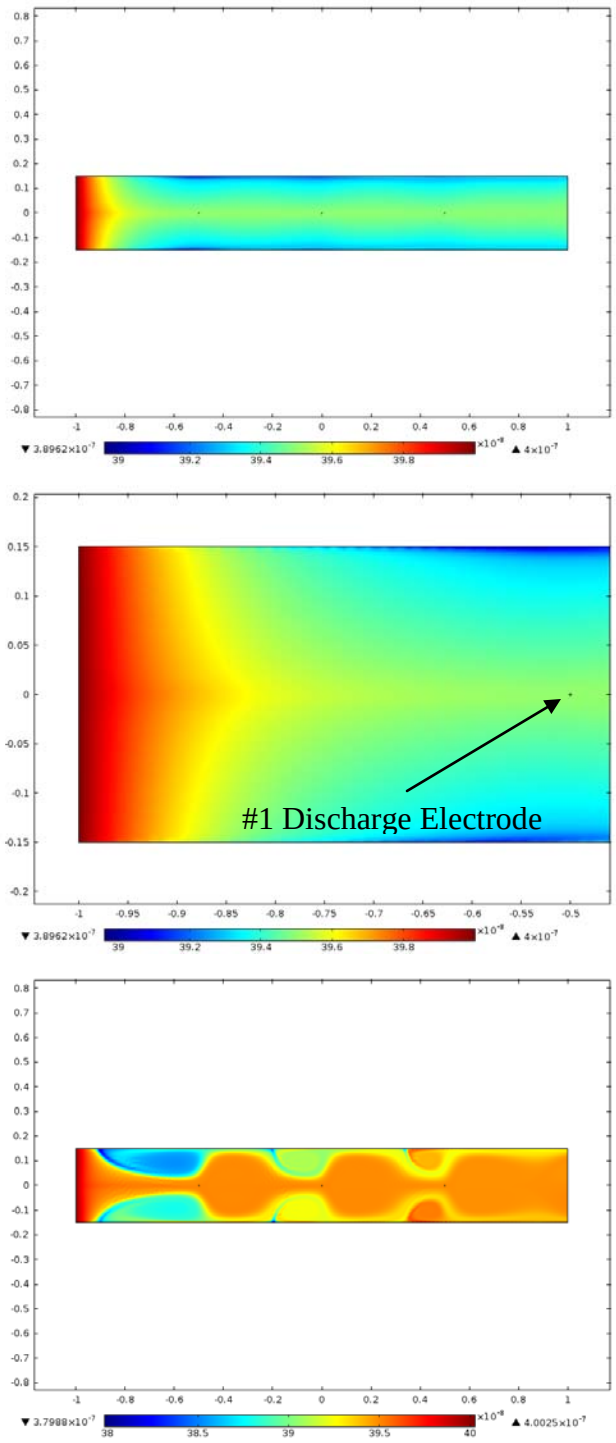

Figure 6. Computed distributions of mercury concentration for adsorption by only polydisperse suspended particles (1.5-125 μm, injection rate of 6 lbs/MMacf). V_0 = 70 kV, T = 180 ^oC. Upper: Low-EHD condition; mercury removal efficiency of 1.55%. Center: Detail of low-EHD condition. Lower: High-EHD condition; mercury removal efficiency of 1.7%

approaching those maintained in the centerline "jet" flow. Integration of mercury flux over the section inlet and outlet yield a mercury removal efficiency of about 1.7%, greater than that determined for the low-EHD condition but not as significant an improvement in performance as was observed for the wall-bounded calculations (Figure 4). It is clear, however, that particle removal rates for the suspended particle computations play an important role in the removal efficiency; to the extent that the present simulations predict high rates of particle removal near the inlet to the section, severely limited time and surface area for adsorption will consequently limit any performance differences between low- and high-EHD conditions. Or, equivalently, the homogeneous mercury concentration boundary condition at the surfaces of the collection electrodes result in overprediction of mercury removal efficiencies and differences in efficiencies between low- and high-EHD conditions.

CONCLUSIONS

Two-dimensional simulations of the electrohydrodynamically-influenced adsorption of trace flue gas species, such as toxic mercury released during coal combustion, have provided new and valuable insight into the process. Increasing the EHD effect, either by increasing applied voltage or decreasing gas velocity, has the effect of increasing both particle collection and trace pollutant adsorption, via either in-flight or wall-bounded adsorption mechanisms. Such results can provide the foundation for future improvements and optimization of ESPs for simultaneous control of PM and trace metals, in support of growing global interest in reducing mercury emissions.

REFERENCES

1. U.S. EPA (2012). Mercury and Air Toxics Standard. *Federal Register 78* (79).
2. Pavlish, J.H., E.A. Sondreal, M.D. Mann, E.S. Olson, K.C. Galbreath, D.L. Laudal, S.A. Benson (2003). Status review of mercury control options for coal-fired power plants. *Fuel Proc. Technol.* **82**, 89-165.

3. Clack, H.L. (2012). Estimates of Increased Black Carbon Emissions from Electrostatic Precipitators during Powdered Activated Carbon Injection for Mercury Emissions Control. *Environ. Sci. Technol.* **46**, 7327-7333.
4. Clack, H.L. (2006). Mass transfer within electrostatic precipitators: trace gas adsorption by sorbent-covered plate elecdtrodes. *J. Air Waste Manage. Assoc.* **56**, 759-766.
5. Clack, H.L. (2006). Mass Transfer within ESPs: In-flight Adsorption of Mercury by Charged Suspended Particulates. *Environ. Sci. Technol.* **40**, 3617-3622.
6. Clack, H.L. (2006). Particle Size Distribution Effects on Gas-Particle Mass Transfer within Electrostatic Precipitators, *Environ. Sci. Technol.* **40**, 3929-3933.
7. Clack, H.L. (2006). Bimodal Fly Ash Distributions and Their Influence on Gas-Particle Mass Transfer During Electrostatic Precipitation. *Fuel Proc. Technol.* **87**, 987-996.
8. Scala, F. and H.L. Clack (2008). Mercury Emissions from Coal Combustion: Modeling and Comparison of Hg Capture in a Fabric Filter versus an Electrostatic Precipitator, *J. Haz. Mat.* **152**, 616-623.
9. Clack, H.L. (2009). Mercury Capture within Coal-fired Power Plant Electrostatic Precipitators: Model Evaluation. *Environ. Sci. Technol.* **43**, 1460-1466.
10. ADA-ES. Pleasant Prairie Power Plant Unit 2 - Sorbent Injection into a Cold-side ESP for Mercury Control. Final Report; U.S. Department of Energy, May, 2003.